RESEARCH ARTICLE

WILEY

Influence of soil plasticity models on offshore wind turbine response

Gerard V. Ryan[1] [iD] | Thomas A. A. Adcock[1] | Ross A. McAdam[2]

[1]Department of Engineering Science, University of Oxford, Oxford, UK

[2]Department of Geotechnical Design, Ørsted Wind Power, London, UK

Correspondence
Gerard V. Ryan, Department of Engineering Science, University of Oxford, Oxford, UK.
Email: gerard.ryan@eng.ox.ac.uk

Abstract

While recent numerical modelling advances have enabled robust simulation of foundation hysteresis behaviour, uptake of these models has been limited in the offshore wind industry. This is partially due to modelling complexity and the unknown influence of including such soil constitutive models within a design philosophy. This paper addresses this issue by outlining a framework of an aero-hydro-servo-elastic offshore wind turbine model that is fully coupled with a multisurface plasticity 1D Winkler foundation model. Comparisons between this model and industry standard aeroelastic tools, such as OpenFAST, are shown to be in good agreement. The hysteretic soil predictions are also shown to be in good agreement with CM6 Cowden PISA test piles, in terms of secant stiffness and loop shape. This tool has then been used to address the unknown influence of hysteretic soil reactions on the design of monopile supported offshore wind turbines against extreme conditions. This study demonstrates that a significant reduction in ultimate and service limit state utilization is observed when a multisurface plasticity foundation model is adopted, as opposed to industry standard pile–soil interaction models.

KEYWORDS
aeroelastics, BSH storm, monopile, multibody dynamics, SLS, soil damping, ULS

1 | INTRODUCTION

The dynamic behaviour of an offshore wind turbine (OWT), which is a key driver of the material cost for the structure, is heavily dependent on the stiffness and damping of the restraining foundation. Monopile designs using existing standards were typically modelled using linear or p–y springs which do not include changes in soil stiffness during unload and reload events. As such, they do not replicate observed foundation behaviour.[1] Subsequent poor prediction of foundation behaviour led to the development of a range of improved numerical models for OWT monopiles such as HARM,[2] REDWIN,[3] and PIMS.[4] These improved models all inherently capture hysteretic soil behaviour, while some capture additional ratcheting, rate, and gapping effects. While these new models are currently being validated through extensive experiments, such as the PICASO programme,[1] the holistic importance of using such models within a design framework is not yet fully understood. Therefore, a robust assessment of how significant the current absence of hysteretic soil reactions on OWT design is needed.

The design of OWTs relies heavily on aero-hydro-servo-elastic codes to simulate the most significant conditions that an OWT may experience. These coupled time-domain-based tools take into account the interaction of various environmental conditions with the entire structural assembly of the turbine, for example, a sudden gust of wind causing a change in blade pitch which in turn reduces the structural load.

Various tools exist today to simulate OWT dynamics. However, the base versions of each tool use simplified foundation models consisting of either linear or plastic p–y springs as outlined in Malekjafarian et al.[5] and illustrated in Table 1. Therefore, these tools do not capture the observed phenomenon of soil hysteretic behaviour. While recent work has begun to investigate the influence of soil hysteresis on the design of OWTs,[3] this work focussed on fatigue limit state for a 5 MW turbine and uses a macrobased formulation of the foundation, which omits simulation of the behaviour below mudline. A more common approach in industry is to use a set of Winkler springs, allowing analysis of the foundation below the mudline.

The ability to model this interaction between embedded monopile behaviour and aeroelastic loading is likely to be important for capturing the hardening, rate dependent, and ratcheting behaviour of advanced cyclic soil reaction models, such as HARM[8] or HCA.[9] Capturing this interaction below mudline will allow a more accurate prediction of OWT response when subjected to environmental loading thereby reducing design uncertainty and improving efficiency. In addition, the proposed size of OWTs at present is a significantly different design scenario to a 5 MW turbine; current monopile designs may be excess of 10 m in diameter supporting 15–20 MW turbines, where pile length-to-diameter ratios (L/D) range between 2 and 4. Ultimate limit state analysis is also becoming a significant design element, given that there is a general trend to deploy in more exposed sites, leading to more treacherous extreme conditions. These extreme storm events typically result in the largest foundation loads which are compounded by low aerodynamic damping levels due to parked turbine conditions. Given that hysteretic soil behaviour is a source of damping which is strongly correlated to load level, these storm circumstances provide exactly the conditions in which the structural response could be critically dependent on hysteretic soil behaviour.

The objective of this paper is to outline a model with the desired capabilities of accurately capturing the dynamics of a modern OWT system while incorporating soil hysteresis through a multisurface soil plasticity 1D Winkler model. In an ideal world, this model would be compared and validated against a set of suitable benchmark results. However, it would be very difficult to create such a benchmark dataset, as small-scale models are not able to accurately reproduce the fluid structure interaction of the aeroelastics and it is very difficult to accurately measure the applied loads for full-scale structures. Consequently, there is not a suitable benchmark dataset and a separate validation of the aeroelastic and pile–soil interaction models represents the most robust validation of the system, given the lack of suitable benchmark data of coupled dynamic response at physically representative scales.

TABLE 1 Overview of methods used within aero-hydro-servo-elastic codes (adapted from the literature[6,7] to include pile–soil interaction models and latest codes).

Code	Aerodynamics (aero)	Hydrodynamics (hydro)	Control (servo)	Structural (elastic)	Pile–soil interaction	Licence
3DFloat	BEM or DW	AiryStr or UD Stream + ME	UD	IFEM	Mac[a]	CM
ADAMS + AeroDyn	BEM or DW + DS + 3DFW	AiryStr or UD or Stream + ME	DLL or UD	MBS	AF, Wink[a,b], Mac[a]	CM
ADCoS-Offshore	BEM DS	AiryStr or UD or Stream + ME	DLL or UD	IFEM	AF, Wink[a]	CM
ASHES	BEM DS	AiryStr + ME	UD or DLL	IFEM	AF, Mac[a], Wink[a,b]	CM
BHawC2	BEM or DW + DS	AiryStr or UD or Stream + ME	DLL or UD	MBS/IFEM + Modal	AF, Mac[a], Wink[a,b]	CM
Bladed	BEM or DW + DS	AiryStr or UD or Stream + ME	DLL or UD	MBS	AF, Mac[a], Wink[a,b]	CM
FAST	BEM or DW + DS + 3DFW	AiryStr or UD + ME	DLL or UD or SM	FEMp + Modal/IFEM	AF, Mac[a]	OS
Flex5	BEM or DW + DS	AiryStr or UD or Stream ME	DLL or UD	IFEM + Modal	AF, Mac[a], Wink[a]	CM
HAWC2	BEM or DW + DS	AiryStr or Stream or UD ME	DLL or UD or SM	MBS/IFEM	AF, Mac[a], Wink[a,b]	CM
OneWind	BEM or DW + DS	AiryStr or UD + ME	DLL or UD	MBS/IFEM	AF, Wink[a,b]	CM
OrcaFlex	BEM + DS	AiryStr + PF + ME	DLL	MBS	AF, Mac[a], Wink[a,b]	CM

Abbreviations: 3DFW, free wake vortex method; AF, apparent fixity; AiryStr, airy theory with stretching method; BEM, blade element momentum theory; CM, commercial; DLL, external dynamic link library; DS, dynamic stall implementation; DW, dynamic wake theory; FEMp, FE for mode preprocessing only; IFEM, incremental finite-element method; Mac, macrobased element at mudline; MBS, multibody dynamics formulation; ME, Morison's equation; Modal, modal reduced system; OS, open source; PF, linear radiation and diffraction; SM, interface to Simulink with MATLAB; Stream, Dean's stream function; UD, user-defined subroutine; Wink, Winkler springs distributed along pile.
[a]Linearized foundation springs.
[b]p–y foundation springs.

Therefore, this paper will provide an overview of this model before presenting separate verification of its aeroelastic and pile–soil interaction performance. This model is then used to address the unknown influence of hysteretic soil reactions on the design of monopile supported OWTs against extreme conditions in terms of ultimate limit state (ULS) and service limit state (SLS) design.

2 | MODELLING FRAMEWORK

The model described in this paper (referred to as OxDyn) extends the OWT dynamic model described by McAdam et al.,[10] which consists of a 1D beam finite element (FE) code designed to simulate the dynamic response of simplified OWT superstructures with advanced foundation soil–structure interaction. The McAdam model did not explicitly model wind turbine components such as blades and drivetrain and was therefore unable to accurately model full aeroelastic behaviour of an OWT.

2.1 | Multibody modelling

OWT structural components have been formulated using the multibody dynamics approach, which has been extensively verified by the aircraft and space industry.[11] In total, seven bodies are used to define the system, consisting of the support structure (tower and monopile), yaw bearing, shaft, hub, and a separate body for each individual blade. A breakdown of the various coordinate systems (CS) adopted for each body is given in Table 2 and is illustrated in Figure 1. The orientation each of these bodies is described using the XYZ sequence of Euler angles which allows exact representation of large rotations.[12]

The floating reference frame approach (FRF) as outlined in Shabana[12] has been used to describe the kinematics of flexible blades, where each FRF is at the root of the blade and its z-axis is aligned with the blade pitch axis.

It is noted that Euler angles suffer from singularity at certain orientations; however, the current chosen XYZ sequence means that this singularity only would occur for unrealistic wind turbine orientations. For example, the shaft frame of reference is orientated such that the x-axis is parallel to the rotor axis of rotation as illustrated by Figure 1. Therefore, for this singularity to occur requires the turbine to deflect such that the

TABLE 2 System coordinate types.

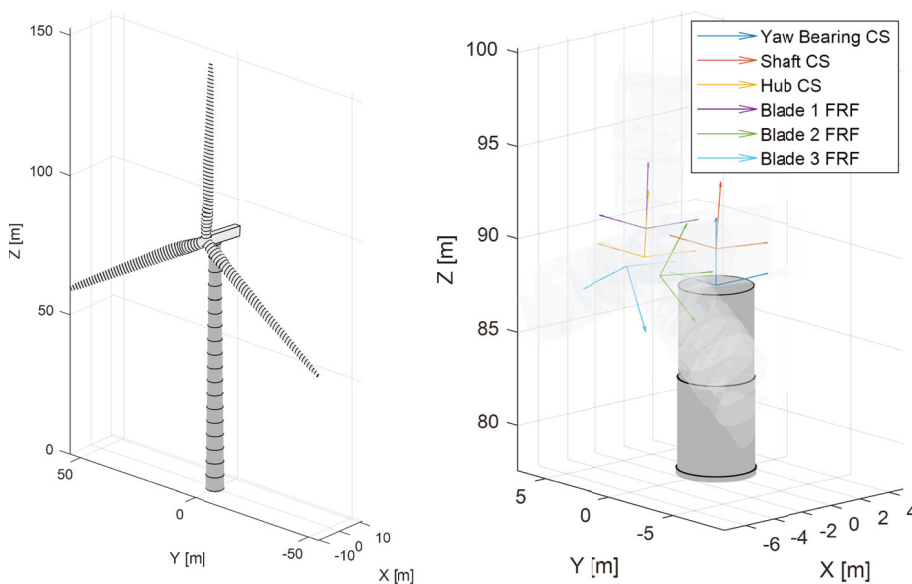| Coordinate type	Support structure	Yaw bearing	Shaft	Hub	Blades
Reference translation (R)	—	✓	✓	✓	✓
Reference orientation (θ)	—	✓	✓	✓	✓
Elastic deformation (f)	✓	—	✓	—	✓

FIGURE 1 Wind turbine system multibody configuration and coordinate systems.

shaft axis of rotation is approximately 90° from the original orientation, for example, the shaft axis would need to be vertical at either 0 or 180 azimuth angle.

2.2 | Equations of motion

The method of Lagrange multipliers (see Shabana[12]) has been used to describe the motion of the interconnected wind turbine system leading to the following set of ordinary differential equations:

$$
\begin{bmatrix} \mathbf{M} & \mathbf{C}_q^T \\ \text{symmetric} & 0 \end{bmatrix} \begin{bmatrix} \ddot{\mathbf{q}} \\ \lambda \end{bmatrix} + \begin{bmatrix} \mathbf{C} & 0 \\ 0 & 0 \end{bmatrix} \begin{bmatrix} \dot{\mathbf{q}} \\ 0 \end{bmatrix} + \begin{bmatrix} \mathbf{K} & 0 \\ 0 & 0 \end{bmatrix} \begin{bmatrix} \mathbf{q} \\ 0 \end{bmatrix} = \begin{bmatrix} \mathbf{Q}_e + \mathbf{Q}_v \\ \mathbf{Q}_c \end{bmatrix}
$$

or more explicitly written in terms of generalized coordinate partitioning:

$$
\begin{bmatrix} m_{RR} & m_{R\theta} & m_{Rf} & \mathbf{C}_{q_r}^T \\ & m_{\theta\theta} & m_{\theta f} & \mathbf{C}_{q_\theta}^T \\ & & m_{ff} & \mathbf{C}_{q_f}^T \\ \text{sym} & & & 0 \end{bmatrix} \begin{bmatrix} \ddot{\mathbf{q}}_R \\ \ddot{\mathbf{q}}_\theta \\ \ddot{\mathbf{q}}_f \\ \lambda \end{bmatrix} + \begin{bmatrix} 0 & 0 & 0 & 0 \\ & 0 & 0 & 0 \\ & & \mathbf{C}_{ff} & 0 \\ \text{sym} & & & 0 \end{bmatrix} \begin{bmatrix} \dot{\mathbf{q}}_R \\ \dot{\mathbf{q}}_\theta \\ \dot{\mathbf{q}}_f \\ 0 \end{bmatrix} + \begin{bmatrix} 0 & 0 & 0 & 0 \\ & 0 & 0 & 0 \\ & & \mathbf{K}_{ff} & 0 \\ \text{sym} & & & 0 \end{bmatrix} \begin{bmatrix} \mathbf{q}_R \\ \mathbf{q}_\theta \\ \mathbf{q}_f \\ 0 \end{bmatrix} = \begin{bmatrix} (\mathbf{Q}_R)_e + (\mathbf{Q}_R)_v \\ (\mathbf{Q}_\theta)_e + (\mathbf{Q}_\theta)_v \\ (\mathbf{Q}_f)_e + (\mathbf{Q}_f)_v \\ \mathbf{Q}_c \end{bmatrix},
$$

where the subscripts R, θ, and f are the reference position, orientation, and deformation, respectively.

$\mathbf{M}$ is the mass matrix, $\mathbf{q}$ is the generalized coordinates of the system, $\mathbf{Q}_e$ is the vector of generalized forces, $\mathbf{Q}_v$ is the quadratic velocity vector that includes velocity-dependent inertia forces, and $\mathbf{K}_{ff}$ and $\mathbf{C}_{ff}$ are the FE stiffness and damping matrices.

The kinematic constraints, which describe connectivity between components, are expressed in terms of nodal accelerations leading to the Jacobian matrix $\mathbf{C}_q$ and vector of velocity-dependent terms $\mathbf{Q}_c$ as outlined in Shabana.[12] The resulting joint forces due to these constraints are conveniently expressed in terms of $\mathbf{C}_q$ and a set of yet unknown Lagrange multipliers λ that can be solved for along with the system accelerations.

2.3 | System mass

The monopile and tower is modelled using Timoshenko beam theory[10,13] formulated using four-point Gauss integration. The nacelle assembly is modelled as a lumped mass and inertia, offset from the top tower node. The remaining components of the shaft, hub, and blades all undergo large rotations with respect to the inertial coordinate system. Therefore, due to the noncommutative behaviour of finite rotations, special care has been taken to correctly model the nonlinear inertia of the system by updating the mass matrix at every timestep. This is efficiently implemented by means of precomputed inertia shape integrals.[12]

2.4 | System stiffness

The stiffness matrix for the blades is modelled using classical Euler–Bernoulli beam theory due to the blades being long and slender. However, monopile and tower stiffness is modelled using Timoshenko beam theory, as outlined in Friedman and Kosmatka[13] and McAdam et al.[10] As with typical beam theory, small deformations are assumed which allows omission of higher order terms. These higher order terms couple bending with axial deformation and become more significant with increasing axial force. As blades experience large centrifugal forces, this coupling can be significant for operating conditions.[14] To include this coupling, a geometric stiffness matrix as outlined in Gavin[15] is implemented. As the dominant axial force for blades is caused by centrifugal forces, these corrections are sometimes termed centrifugal stiffening. A similar geometric destiffening effect, due to gravity loading, is also implemented in the support structure.

2.5 | System damping

Rayleigh damping[16] has been used to model the internal structural energy dissipation. Consequently, the amount of damping modelled varies as a function of response frequency; however, structural damping is generally assumed to be independent of frequency.[17] Therefore, to ensure that

the appropriate amount of structural damping is captured across the range of dominant response frequencies, damping ratios at the 1st and 13th modal frequencies are specified, which preserves the exact damping ratio at the dominant first tower mode and the 13th mode, for example, second tower or second blade mode. Damping in between these two specified frequencies will be slightly lower; however, this selection will result in a conservative estimate of the dynamic response. Other sources such as aerodynamic and soil damping are not modelled using Rayleigh damping. These are inherently captured in the mechanics of the model which are discussed in later sections of this paper.

2.6 | Hydrodynamics

Forces from wave and current kinematics are calculated using Morison's equation with MacCamy–Fuchs corrections as recommended by the International Electrotechnical Commission.[18] A steady current model is applied codirectional with the wavefield, where the velocity shear profile is based on the one-seventh power law. These kinematics are superimposed with the wavefield, which is modelled using linear random wave theory and the JONSWAP spectra. Linear random wave theory produces large errors near the water surface due to incorrect extrapolation of high-frequency components above the associated individual amplitudes, otherwise known as high-frequency contamination.[19] To mitigate against this overprediction of kinematics, stretching[20] has been used. In addition to this, stream function wave theory has been implemented following Dean[21] to accurately model nonlinear regular waves.[18]

2.7 | Aerodynamics

Loads acting on the rotor are calculated using blade element momentum theory (BEM). An unsteady multistream tube BEM method is adopted which closely follows Hansen.[22] The motion of the blades is described using a complete description of element orientation and velocity, for example, the relative velocity includes components due to tower and blade deformation. Industry standard BEM corrections are also applied, consisting of tower shadow effects,[23] Prandtl's tip and hub loss,[24] Glauert thrust,[25] yaw/tilt,[26] dynamic stall,[27] and wake corrections.[28] Aerodynamic forces acting on the tower are calculated using the incident wind field with a drag coefficient of 0.9.

In addition to steady wind fields, TurbSim has been used to model stochastic wind fields, which incorporate effects of turbulence and wind shear.[29] A Kaimal spectrum has been adopted for simulations in this paper, as recommended by IEC.[18]

2.8 | Control system

The control system utilizes the ROSCO controller developed by Abbas et al.,[30] which is capable of modelling conventional variable-speed and variable blade-pitch-to-feather control routines, such as those employed for the NREL 5 MW and IEA 15 MW turbines. ROSCO has been coupled with the aeroelastic model via an external DLL.

2.9 | Time integration

Linear and nonlinear implementations of the Newmark Beta approach[31] are used to implicitly integrate the equations of motion in time using the standard prediction–correction procedure, with $\gamma = 0.5$ and $\beta = 0.25$. In the nonlinear method, the soil stiffness is displacement dependent; thus, the equations of motion are iteratively solved within a tolerance, using a Newton Raphson method. Specifically, the external force vector is balanced with the nonlinear internal force vector plus the inertia of the system.

Numerical integration of the constraint equations causes errors to accumulate in the joint coordinates. Therefore, to prevent this, the constraints are eliminated from the equations of motion using the velocity transformation method outlined in Géradin and Cardona.[32]

2.10 | Soil–monopile interaction

Many approaches are available to model the monopile soil–structure foundation behaviour, with those most commonly applied in beam element modelling, following the Winkler springs approach. Two realizations of this model are presented in this paper, one with linear and one with nonlinear (p–y) stiffness. In addition, a third model is presented that uses an 'Iwan style' parallel spring-slider method, as illustrated in Figure 2 (left). This multisurface plasticity method can capture both nonlinear stiffness and hysteretic response which closely follows the work of Whyte et al.[4] The Iwan model consists of a set of n parallel spring sliders at every Gauss point along the embedded pile. Each spring slider has a linear
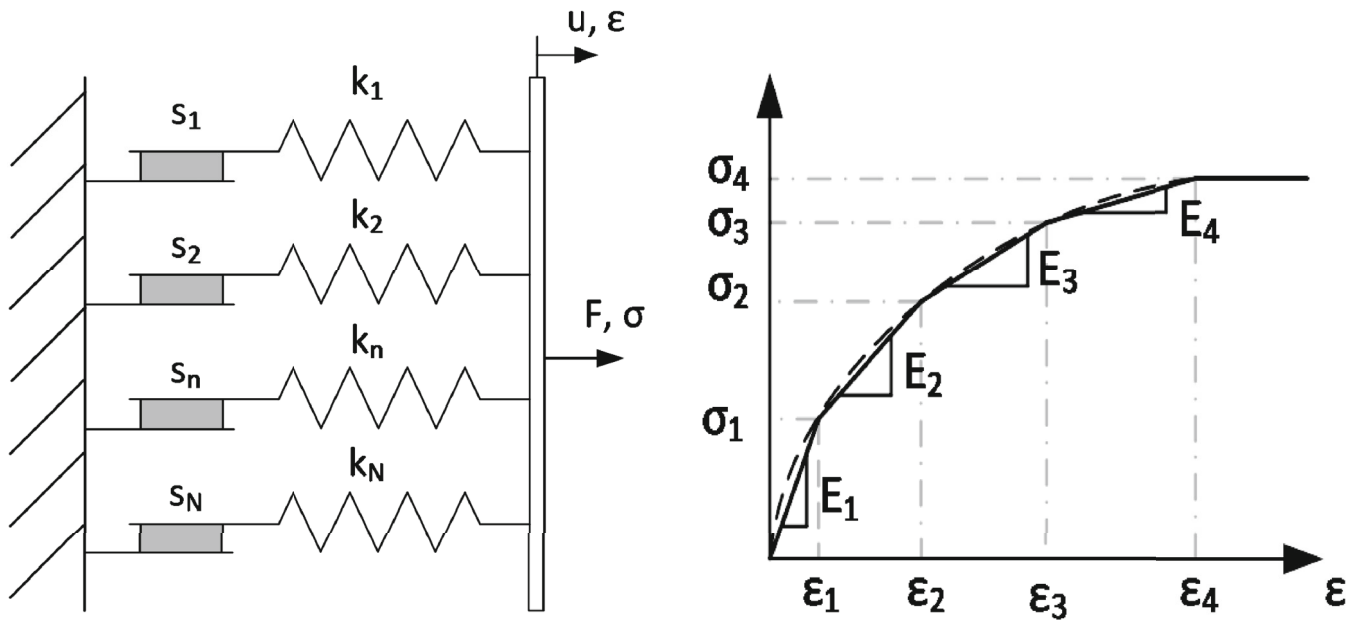
FIGURE 2 Parallel spring-slider analogy (left) and multilinear behaviour (right).

stiffness, k_n, and associated capacity, s_n, which act in an elastic perfectly plastic behaviour resulting in a stress–strain response that is multilinear, as illustrated in Figure 2 (right).

The target reaction behaviour (illustrated by the black dashed line in Figure 2, right) is discretized into a number of linear steps, equal to the number of elements/yield surfaces N_{surf} in the Iwan model. The element strength and stiffness parameters are then calculated as

$$k_n = \frac{(\sigma_n - \sigma_{n-1})}{(\varepsilon_n - \varepsilon_{n-1})} - \sum_{i=n+1}^{N_{surf}} k_i \qquad s_n = k_n \varepsilon_n$$

These stiffness and capacity parameters are calibrated to match the target backbone monotonic shape of the relevant p–y curve at the embedment of interest, whereby a sufficiently large number of spring sliders are adequate to replicate a smooth p–y curve, for example, 20 spring sliders per Gauss point. The capacity of each spring slider is characterized in stress space by a circular yield surface in the x–y plane (fore-aft–side-to-side) of radius s_n as shown by Figure 3 (left).

During a timestep, the displacement vector is incremented in order to calculate the corresponding stress. Figure 3 (left) illustrates the changes in stress during a solution increment. The stress is initially estimated using a trial displacement increment, assuming an elastic response of the local element. If the estimated stress is within the yield surface, this stress is allocated to the spring slider. However, if the stress is outside the yield surface, then the spring slider is plastic, and the stress tracks back radially to sit on the yield surface. The important functionality of this model is that if a load is reversed, the stress point for each spring slider moves inside the yield surface, resulting in regained stiffness and reproducing the commonly observed hysteretic behaviour illustrated in Figure 3 (right).

3 | BENCHMARK CODE COMPARISON

3.1 | Eigen value validation

To validate the aeroelastic performance, modal properties predicted using OxDyn are compared against Phase 1 of the international Offshore Code Comparison Collaboration (OC3) Project.[33] For this analysis, the system consisted of the NREL 5 MW baseline wind turbine,[34] mounted atop a 6 m diameter monopile in 20 m water depth, which is fixed at seabed, that is, no soil stiffness is included. Table 3 lists the predictions of the first 10 modes for OxDyn and various industry standard codes, along with the mean of all benchmark codes that participated in the OC3 Project Phase 1. The OxDyn model predictions consistently lie within the range of benchmark code predictions. Small variability is introduced by differing theories implemented in the various codes. Notably, the biggest difference exists in mode 9, which is the blades second asymmetric
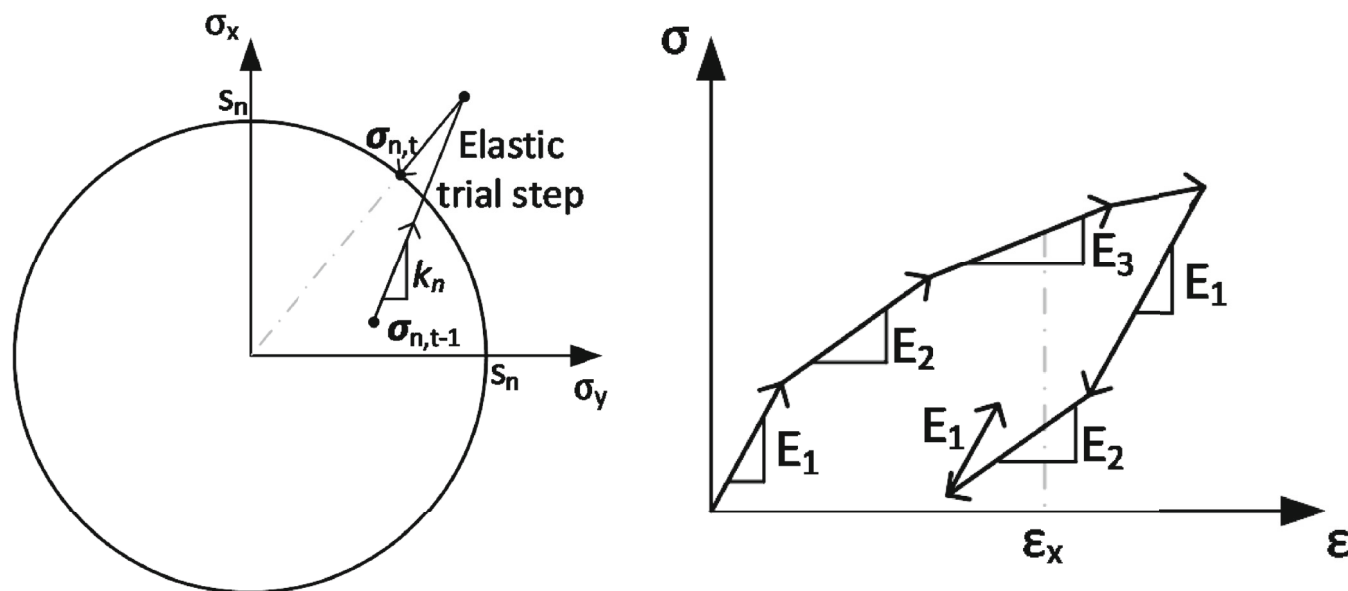
FIGURE 3 Stress evolution for a single element/surface during a solution increment (left) and load–unload–reload behaviour (right).

flapwise yaw mode, where yaw refers to the coupling of blade asymmetric modes with the nacelle–yaw motion. This discrepancy is due to OxDyn and ADAMs modelling tower torsion, whereas OpenFAST and Bladed do not model this degree of freedom.[33]

3.2 | Uniform wind load case validation

To validate the time domain prediction of aeroelastic behaviour, OpenFast and OxDyn simulations have been compared with both uniform steady and spatially varying stochastic cases using the NREL 5 MW baseline wind turbine.[34] Figure 4 show the predicted aeroelastic loads and response, respectively, for a 10 m/s uniform wind load case. Two variations of the OpenFast model have been presented: ElastoDyn, which represents the blades with two flapwise and one edgewise mode shape based on Euler–Bernoulli beam theory (no torsion); and BeamDyn, which represents the blades with 48 geometrically exact Legendre spectral beam elements that better model geometric nonlinearities and large deflections. The torque acting on the main shaft is split into two components: aerodynamic representing the torque due to the aerodynamic forces acting on the blades and electrical representing the reaction torque from the generator. OxDyn displays good fidelity in both transient response and steady-state response, matching the torque, thrust, rotation rate, and blade displacements. These indicate that the forces, stiffness, mass, damping, and controller of the system are well captured.

3.3 | Stochastic wind load case validation

To further validate the time domain aeroelastic simulation, a 16 m/s turbulent wind load case was compared against OpenFAST, as shown in Figure 5. Note that all BEM corrections previously described were applied in this simulation. The 1P frequency has been obtained by taking the mean of the simulated rotor rotation frequency over the length of simulation period. The passing frequency (3P) is simply found by multiplying the 1P by 3 to account for the number of blades. Higher order load frequencies (6P and 9P) also excite the support structure at integer multiples of the 3P frequency which are also shown in Figure 5.

Again, OxDyn displays good fidelity in the aerodynamic thrust loading, in particular at the support structure excitation frequencies (3P to 9P). The consistency in 3P loading indicates that the periodic force on each blade due to gravity, shaft tilt, and wind shear is being captured, while the agreement at 6P and 9P loading also suggests that the tower shadow effects are being captured accurately.

Subsequently, the peaks in the nacelle displacement at 3P, 6P, and 9P indicate that the correct loads are being transferred from the blades to the hub, shaft, yaw bearing, and into the tower. In addition to this, the close agreement at 1P shows that there is no rotor imbalance and that the kinematic constraints in the multibody formulation are capturing the appropriate dynamics.

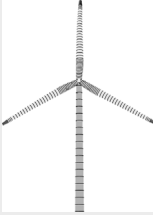**TABLE 3** Simulated modal properties using OxDyn and various benchmark codes.
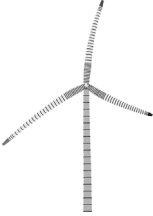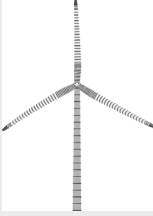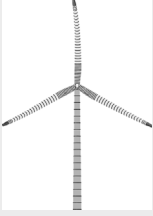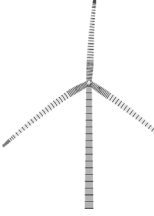
Description	Simulated frequencies (Hz)				Benchmark	OxDyn simulated mode shapes		
	OxDyn	OpenFAST	ADAMS	Bladed	Mean (Hz)	Front view	Side view	Top view
First tower Side-to-side	0.275	0.280	0.277	0.273	0.279			
First tower Fore-aft	0.278	0.282	0.279	0.282	0.279			
First drivetrain Torsion	0.601	0.617	0.600	0.606	0.614			
First blade asymmetric Flapwise yaw	0.628	0.663	0.621	0.701	0.646			
First blade asymmetric Flapwise pitch	0.663	0.669	0.664	0.688	0.670			
First blade Collective flap	0.697	0.700	0.700	0.726	0.692			
First blade asymmetric Edgewise pitch	1.074	1.077	1.072	1.086	1.075			

TABLE 3 (Continued)

| Description | Simulated frequencies (Hz) | | | | Benchmark | OxDyn simulated mode shapes | | |
	OxDyn	OpenFAST	ADAMS	Bladed	Mean (Hz)	Front view	Side view	Top view
First blade asymmetric Edgewise yaw	1.088	1.092	1.086	1.102	1.089			
Second blade asymmetric Flapwise yaw	1.693	1.929	1.607	1.995	1.764			
Second blade asymmetric Flapwise pitch	1.805	1.885	1.799	1.838	1.828			
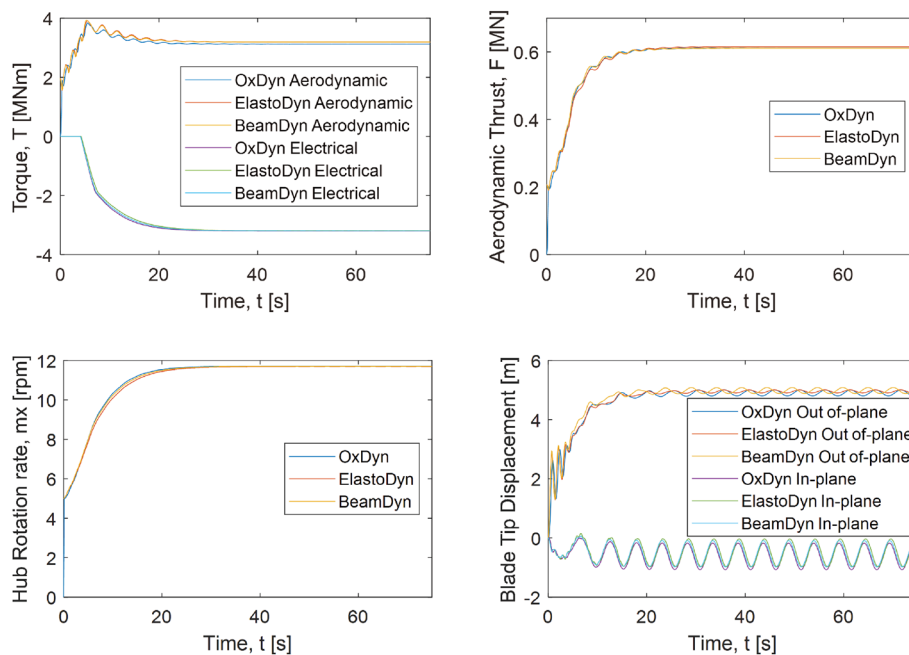
FIGURE 4 Uniform wind aeroelastic load and response comparison with OpenFAST (ElastoDyn and BeamDyn).

4 | EXTREME CONDITIONS STUDY

The ability to holistically model the aeroelastic behaviour of the superstructure and varying levels of embedded foundation complexity, such as the inclusion of plasticity and hysteresis, allows quantification of pile–soil interaction model influence on OWT design. Wind turbine generator (WTG) design is typically conducted using linear foundation springs and the substructure is designed with either linearized or p–y springs, such as
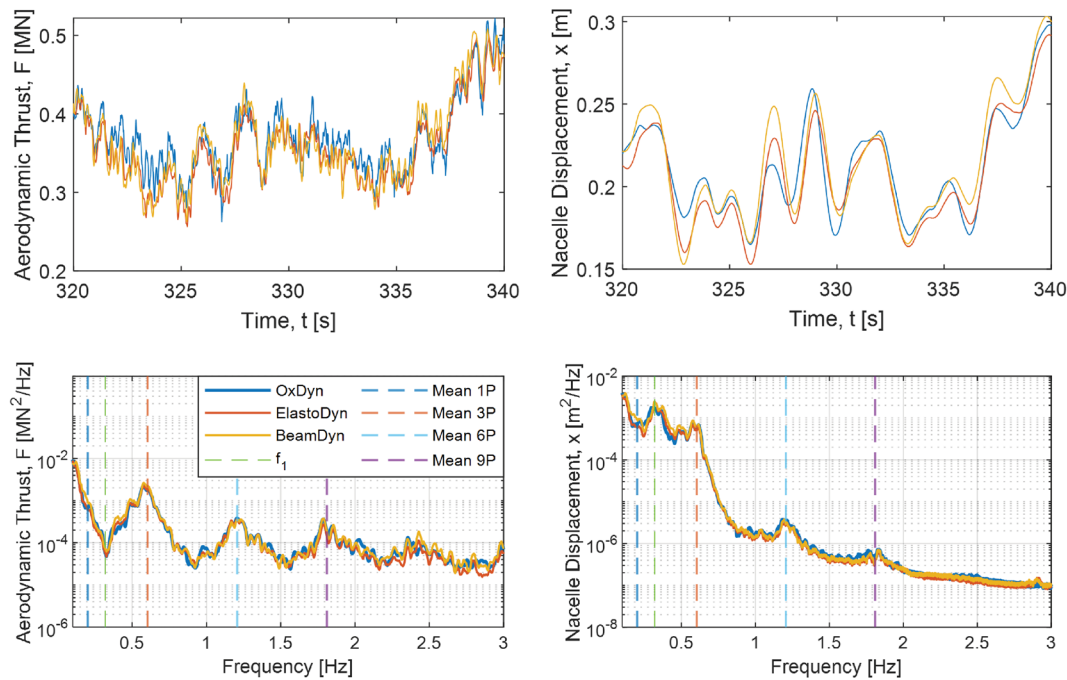
FIGURE 5 Stochastic wind load case comparison with OpenFAST (ElastoDyn and BeamDyn).
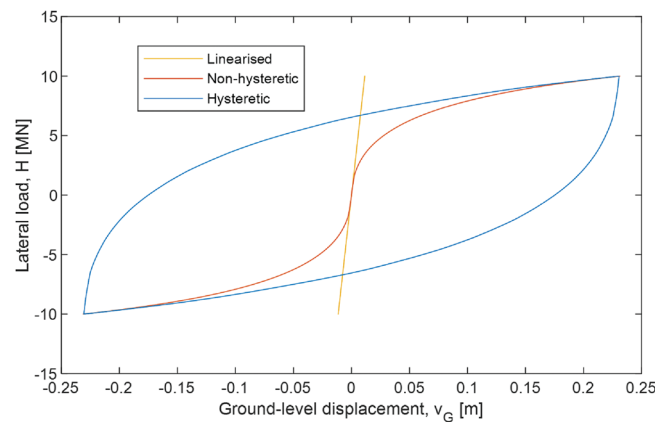
FIGURE 6 Displacement response to cyclic load for each foundation model.

the PISA rule-based design method used in this study, where the PISA rule-based parameters have been verified to capture large pile diameter effects up to 10 m in calibration space.[35]

Therefore, to demonstrate the potential of coupling an aeroelastic tool with hysteretic reactions of the embedded foundation, a study on ultimate limit state (ULS) and service limit state design (SLS) is presented for various foundation models. Specifically, three soil models were considered, each of which are described below and illustrated in Figure 6:

1. 'Nonhysteretic method': Four separate nonlinear soil reaction components are considered at the pile–soil interface capturing the virgin backbone monotonic response based on the PISA design method,[35] two per Gauss point (accounting for distributed lateral load and moment) and two at the base of the monopile (base horizontal force and moment). These capture the combined action of the lateral soil resistance and shear along the pile shaft and base. This model is often seen as the industry standard for ULS design given that it can capture the backbone response and subsequently pile ultimate capacity.

2. Linearized: Each spring in the PISA-based method is linearized using the initial tangent stiffness of the soil reaction curve. This method is the most efficient of all models as it does not require updating at each timestep. Hence, it is almost always used for fatigue analysis.

3. 'Hysteretic method': Each nonlinear soil reaction component in the PISA method is used to generate 20 Iwan 'style' springs at each embedded Gauss point and at the base. These sets of spring sliders capture the backbone and hysteretic Masing behaviour at each embedment location. This is therefore deemed to be the most accurate model of all three cases. Note that due to the mechanics of this method dictating a change in soil stiffness during unload and reload, hysteretic damping is inherently incorporated within the model, being equal to the enclosed area of the loop shown in Figure 6.

4.1 | Wind turbine and site description

The reference site for this study was chosen to represent a typical location in the North Sea of a water depth of 45 m. The soil conditions consist of a homogenous over consolidated clay that match the idealized Cowden profile, as described in Byrne et al.[36] and summarized in Figure 7.

The turbine used for this study is the IEA 15 MW turbine as outlined in Gaertner et al.[37] The main properties of this turbine are summarized in Table 4. However, the monopile and tower geometries have been adjusted, to better represent recent installations of monopiles, whereby a pile embedment of 35 m is used along with a conical section below mean sea level to reduce hydrodynamic loading. An illustration of the corresponding diameter and wall thickness variation is given in Figure 8.

4.2 | Cyclic degradation and ratcheting model

It is well established that when soils are subjected to moderate cyclic loading, they undergo changes of stiffness, strength, and damping. These effects can depend on loading rate and past history as well as load amplitude. When the loading is biased in one direction, 'ratcheting' displacements may accumulate. Many cyclic response models assume that cyclic loading, such as that during a storm event, causes a change in the subsequent monotonic response.
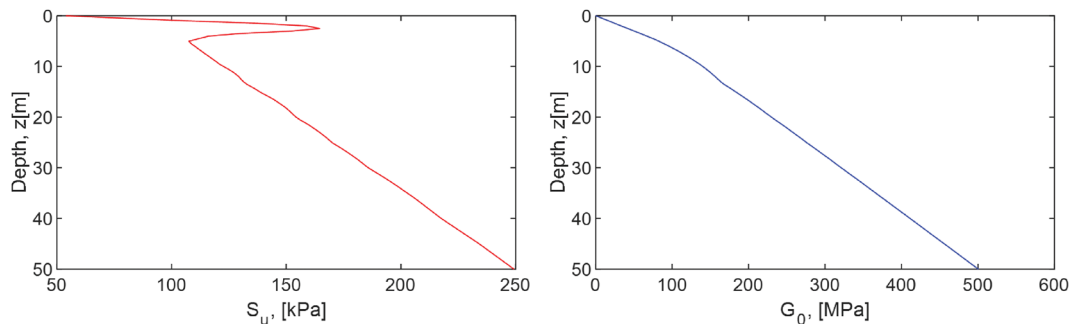
FIGURE 7   Depth-wise Cowden undrained shear strength (left) and small strain shear stiffness (right).

TABLE 4   Summary of IEA 15 MW wind turbine properties.[37]

Parameter	Value
Rated power	15 MW
Cut in, rated, and cut out wind speed	3, 10.59, and 25 m/s
Turbine class	IEC Class 1B
Rotor diameter	240 m
Design tip-speed ratio	9.0
Rotor speed range	5.00–7.56 rpm
3P excitation range	0.250–0.378 Hz
Rotor-nacelle assembly (RNA) mass	950 t
Blade mass	68 t
First blade flapwise natural frequency	0.555 Hz
First blade edgewise natural frequency	0.642 Hz
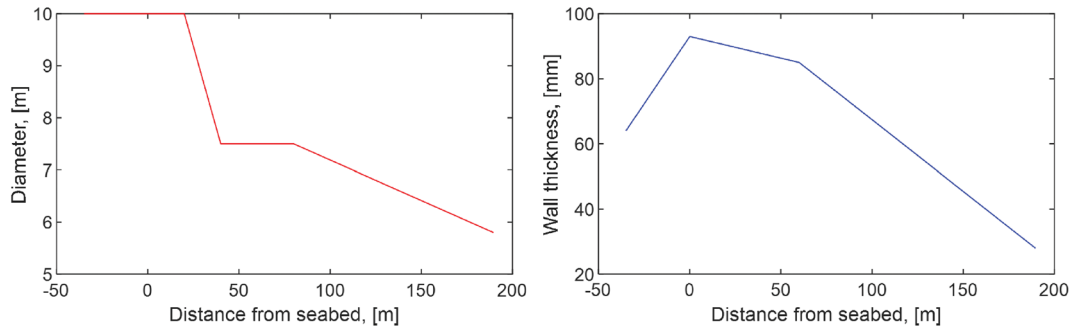
FIGURE 8 Monopile and tower diameter (left) and wall thickness (right) versus distance from seabed.

Evidence of these changes in stiffness, damping, and ratcheted displacement are shown in medium-scale experiments conducted in the PISA project.[38] Typical methods for modelling these effects with North Sea clay soils consist of the API approach,[39] the NGI approach[40], and more recently HARM.[2] The API method for clay consists of limiting the ultimate capacity of the p–y curves to 0.72 times the associated static value. However, this method is therefore independent of loading amplitude, rate, and history. As a result, it would likely give rise to a crude estimation of the site- and turbine-specific ratcheting. The most common approach in industry, the NGI method, is based on cyclic strain diagrams which account for amplitude and cumulative effects by including the number of cycles and loading characteristics such as load amplitude and mean load effects. Development of these cyclic strain diagrams is made through extensive lab testing, which is not publicly available for the Cowden clay profile. Therefore, this study adopts an intermediate method as outlined in Carswell et al.,[41] which is calibrated to match the accumulated rotation of the CM6 Cowden PISA test piles.[38]

In the Carswell method, the ultimate capacity of the virgin monotonic curves at each Gauss point is degraded depending on the number of cycles and displacement at that embedment caused by each load packet through application of a degradation factor λ_N as shown below:

$$P_{uN} = (1 - \lambda_N)P_u \tag{1}$$

$$\lambda_N = \frac{y_{static}}{0.2D} \log(N) \le 1 \tag{2}$$

where P_{uN} is the ultimate resistance after N load cycles, D is the diameter of the monopile, and y_{static} is the static deformation of the monopile. This method assumes the following:

The method initially idealizes the load history at seabed into a set of load packets of increasing magnitude by means of rainflow counting. Then, sequentially applying the degradation rule given by Equations (1) and (2) along with the elastic unload rule to each load packet allows calculation of a degraded 'cyclic' curve and accumulation of rotation. Note that the final residual rotation after a set of one-way loading events can be broken into two components: a static rotation that can be obtained from a nonlinear analysis using standard virgin monotonic springs and an accumulated rotation component which arises due to cyclic effects, that is, a change in soil properties.

To calibrate this method with the CM6 Cowden PISA test results, the degradation threshold was reduced from 50% to 21% which is the mean lateral pile mobilization for the lowest magnitude load packet. Furthermore, a calibration factor based on the ratio of moment utilization was also introduced to the degradation rule as shown in the following equations:

$$P_{uN} = \frac{(1 - \lambda_N)P_u}{\alpha} \qquad \alpha = 0.2324 + 27.94 \cdot \left(\frac{M_i}{M_u}\right)^{4.609}$$

where M_i is bending moment at seabed due to load parcel i and M_u is the ultimate soil moment capacity of the foundation (~2000 MNm for CM6). This power law takes a form similar to LeBlanc et al.,[42] where a power function is also used to consistently predict accumulated rotation in sands. The maximum degradation for stiff clays is commonly taken as 50% of the associated static value above a transition depth (where failure mechanism changes from wedge mechanism to flow around) and 72% below.[43] This transition depth was determined to be greater than the monopile embedment depth of 35 m; therefore, the maximum degradation was capped to 50%.

As shown in Figure 9, the calibrated model accurately predicts the accumulated rotation across all observed load levels. This has been achieved by iteratively adjusting the calibration factor until the accumulated rotation deviates by less than 0.1% from the observed values in the experiments, that is, the difference in initial unload displacement to the unload displacement after a set of load cycles matches the experiment within 0.1%. Note that the match of the absolute unload displacement value is coincidental as the creep during the experiment has offset the
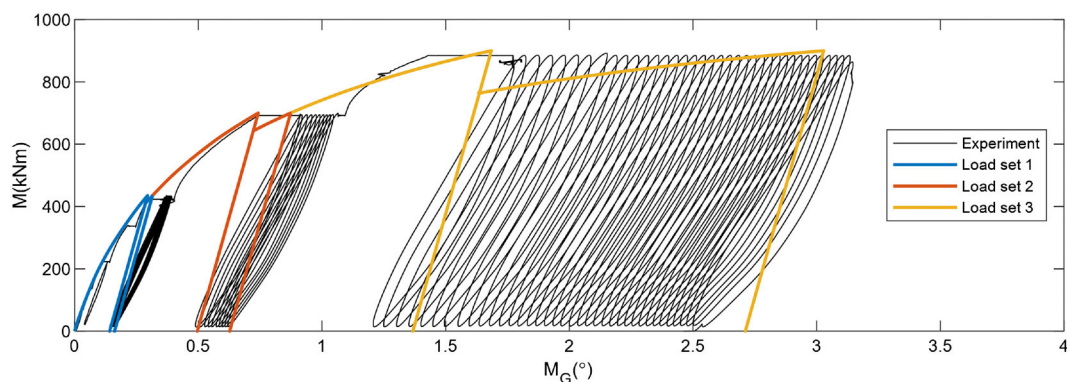
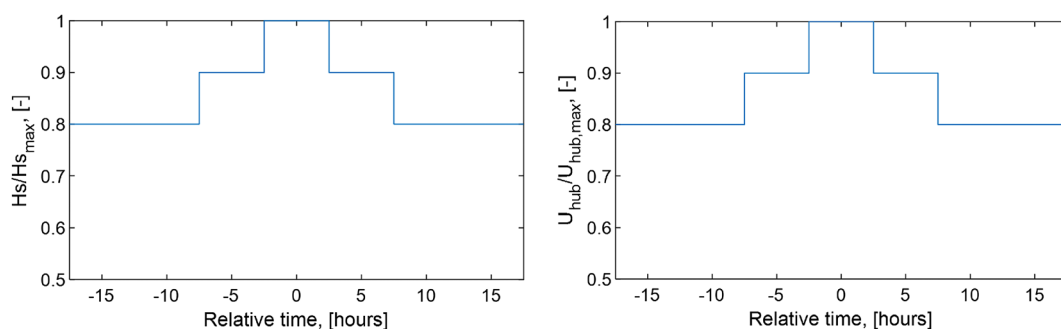**FIGURE 9**   CM6 test results versus calibrated Carswell method.

FIGURE 10   The Bundesamt für Seeschifffahrt und Hydrographie (BSH) storm spectrum.

larger recovery of displacement associated with Masing behaviour. It is also recognized that the peak displacement is underpredicted because the method has been calibrated against the accumulation of unload displacement and an elastic unload stiffness has been assumed in line with standard design practice. A more accurate fit to both the maximum and unload displacements might be achieved if a Masing behaviour unload were adopted.

4.3 | Storm model for cyclic actions

Due to the inherent coupling of ULS and SLS designs with cyclic degradation, it is common in design that a preprocessing stage is conducted whereby a storm event is simulated to get an initial estimate of the seabed load time history which is then used to quantify any changes in soil properties using a cyclic degradation model. This updated soil model is then fed back into the ULS and SLS designs for a final design check where a more accurate representation of response is obtained from the updated soil properties.

The first standard to recommend this process was German BSH guideline,[44] who require use of a 35 h design storm with a build-up, peak, and decay of environmental conditions as shown in Figure 10, where time is defined relative to the extreme wave event. This design storm along with the calibrated Carswell method described in the previous section is used in this study to quantify soil degradation as a result of the storm, allowing calculation of a 'post-cyclic' backbone curve at the end of the 35 h event which is then used to conduct the ULS and SLS design checks for capacity and accumulated deformation.

4.4 | Design load cases

Table 5 provides the list of IEC[18] design load cases (DLCs) used in this study, which often govern ULS and SLS monopile designs. DLC 1.4 simulates an extreme gust condition consisting of a 15 m/s increase in the magnitude of wind speed, along with a wind direction change of approximately 70°, as illustrated in Figure 11 (left). DLC 6.1 simulates an extreme storm event where the structure experiences the largest wave

TABLE 5   IEC and BSH design load cases for foundation model study.

Load case (−)	Mode (−)	U_{hub} (m/s)	I (−)	Hs (m)	Tp (s)	H_{max} (m)	T_{ass} (s)	CS (m/s)	SWL (mMSL)	# sims.
IEC DLC 1.4	Operating	Vr, +2, −2	N/A	1.75	7.5	N/A	N/A	0	0	6
IEC DLC 6.1	Parked	50	ETM	8.5	12.5	16	10.3, 12.3	0.9	3, −1	24
BSH phase 1	Parked	40	ETM	6.8	12.5	N/A	N/A	0.9	0	60
BSH phase 2	Parked	45	ETM	7.65	12.5	N/A	N/A	0.9	0	30
BSH phase 3	Parked	50	ETM	8.5	12.5	16	10.3	0.9	0	30
BSH phase 4	Parked	45	ETM	7.65	12.5	N/A	N/A	0.9	0	30
BSH phase 5	Parked	40	ETM	6.8	12.5	N/A	N/A	0.9	0	60

Abbreviations: CS, current velocity at surface; ETM, IEC extreme turbulence model; H_{max}, extreme wave with 50 year return period; Hs, significant wave height; I, turbulence intensity model; mMSL, relative to mean sea level; phase #, stage of 35 h storm (3 = peak); sims., number of simulations including seeds; SWL, still water level; T_{ass}, wave period associated with H_{max}; U_{hub}, mean hub-height wind speed; Vr, rated wind speed.
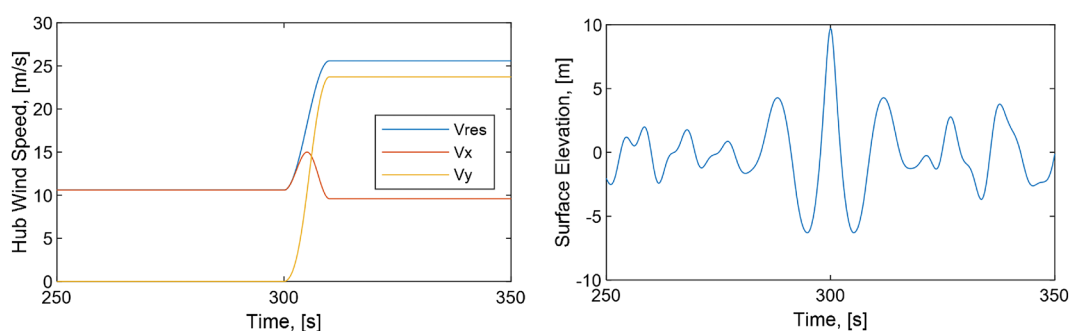
FIGURE 11   DLC 1.4 wind components (left) and DLC 6.1 surface elevation during H_{max} event (right).

expected for a return period of 50 years. This extreme wave is embedded into the 50 year irregular sea state using a constrained nonlinear Stream function wave of 20th order, as illustrated in Figure 11 (right) and described in Rainey and Camp.[45]

These DLCs have been used with the load and resistance factor design (LRD) approach.[18] In addition to the IEC DLCs, properties for each phase of the BSH storm are shown in Table 5, which are simulated with partial safety factors set to 1.

4.5 | Failure criteria

The purpose of the ULS analysis is to verify the structural and the geotechnical resistance of the substructure to extreme loading. Therefore, steel yield and stability (local and global buckling) checks were undertaken in accordance with DNVGL-ST-0126[46] and DNVGL-RP-C202[47] where thickness-dependent yield strengths associated with S355 steel have been obtained from BS EN 10025-2.[48] Furthermore, the utilization ratios were calculated from the seed average of each associated design load case.

The geotechnical load envelope, which defines the boundary of seabed moment versus shear force at which ultimate geotechnical failure occurs, was found to be well approximated by a linear line between the ultimate capacity under pure moment and the ultimate capacity under pure shear, as shown in Figure 15. The capacity envelope boundary was mapped out through separate pushover analyses. The ULS design capacity was then determined by applying a partial safety factor of 1.4 to the envelope in accordance with EN 1997-1.[49] ULS design loads for foundation stability were conservatively taken as the max bending moment and max shear force at seabed during a load event, even though these two maxima may occur at different times.

In the context of monopile foundations, the SLS criterion is defined as the allowable out-of-vertical rotation of the support structure, as discussed in DNV-ST-0126. This is limited to 0.5° by the WTG supplier given that out-of-vertical rotation induces additional periodic loads on the structure (3P, etc.). A 0.25° construction tolerance is typically assumed, leaving an allowable accumulation of rotation of 0.25° over the operating lifetime of the structure. Furthermore, the SLS design loads are commonly calculated from the ULS design load divided by 1.35, to remove the partial load factor.

4.6 | Model parameters

Multidirectional time-domain computations were carried out with distributed loads from gravity, waves, wind, buoyancy, current, and soil reactions, all of which are evaluated at the Gauss points along the structure. These distributed loads are integrated over each element with a Galerkin approach to form consistent forces and moments. Forces and moments arising from permanent and environmental actions are then factored based on the partial load factors given in Table 6. Ten Timoshenko beam elements were used to model the embedded pile, whereas 55 were used to model the remainder of the monopile and tower. In total, 135 Euler–Bernoulli elements were used within the blades, where each Euler–Bernoulli and Timoshenko element has 12 degrees of freedom. All steel components are modelled with a Young's modulus of 210 GPa. The density of the monopile is 7850 kg/m^3, while the density of the tower is 8400 kg/m^3, to account secondary steel such as flanges and bolts. The monopile was modelled with a marine growth density of 1325 kg/m^3 and depth-dependent thickness variation of 100 to 50 mm as per DNVGL-ST-0437.[50]

Each simulation consisted of 800 s in duration, where the first 200 s were removed to mitigate initial transient effects. The structural damping was modelled assuming a damping ratio of 0.6% for the first fore-aft tower dominated mode. This value is based on Shirzadeh et al.,[51] who calibrated this parameter to match long-term measurements of a monopile supported 3 MW OWT in the Belgian North Sea. As structural damping is generally considered independent of frequency, this damping ratio is approximately maintained for the first 13 modes as per the method previously outlined.

The incident wind conditions for turbulent load cases were performed with TurbSim.[52] For the parked cases, the rotor blades were pitched to feather with the rotor brake engaged. The wave kinematics were determined using linear random wave theory and nonlinear Stream function when necessary, that is, DLC 6.1. Each load case has a different wind and wave seed number; however, this seed number was kept consistent for each foundation model. The hydrodynamic loads were calculated using Morrison's equation with drag and inertia coefficients taken as 1.05 and 1.9 which are deemed applicable for Keulegan–Carpenter (KC) numbers corresponding to diameters of 8–10 m with marine growth.[53] An added mass coefficient of 1.0 was assumed which resulted in a natural frequency at the first tower mode of 0.148 Hz.

4.7 | Foundation study results

Table 7 presents the seed averaged ULS design loads at the tower interface and seabed level for each DLC and foundation model considered in this study. Additionally, for DLC 6.1, the design load has been taken as the maximum from the range of water depths and wave periods considered, where the deepest water depth and lowest wave period resulted in the largest loads. This is likely due to the former resulting in a larger lever arm and submerged loading length, whereas the latter results in higher wave kinematics which occur at load frequencies closer to the first tower mode.

TABLE 6 Load factors for extreme event analysis.

Combination	Permanent loads	Environmental loads
ULS	1.10[a]	1.35
SLS	1.00	1.00

[a]Where the permanent load is a favourable load, for example, buoyancy, then has been reduced to 0.9.

TABLE 7 Summary extreme loads of ULS foundation study.

DLC (−)	Model (−)	Maximum Tower interface M_{res} (MNm)	Time coherent Tower interface F_{res} (MN)	Maximum Seabed M_{res} (MNm)	Time coherent Seabed F_{res} (MN)
1.4	Linear	514	4.6	803	2.7
	p–y method	508	4.6	801	4.2
	Iwan method	508	4.6	796	3.9
6.1	Linear	368	4.8	947	12.4
	p–y method	520	6.1	1063	11.5
	Iwan method	441	5.2	937	11.8

Table 7 indicates that the structural loads induced during DLC 6.1 vary more significantly with foundation model than for DLC 1.4. The parked conditions of DLC 6.1 excite a highly dynamic response, where the peak loads occur as part of large dynamic perturbations. The magnitude of these perturbations is dependent on the stiffness and damping of the system, which varies significantly between the different foundation models.

This is demonstrated in Figure 12 which shows a nacelle response time series for DLC 6.1 (left) and the corresponding seed averaged power spectral density (right). The peak in each power spectral density (PSD) indicates the approximate frequency of the first tower mode for the associated foundation model. Figure 12 (right) shows that the first tower mode frequency simulated by the linearized foundation agrees better with the hysteretic model whereas the nonhysteretic method has a peak shifted away from the hysteretic approach. Furthermore, the amount of energy content between each foundation is significantly different.

Figure 13 plots a comparison between the predicted and measured responses of the first load cycle for the first two sets of the CM6 test pile. This simplified scenario could arise due to a mean load from wind and current loading coupled with a cyclic load due to turbulence and wave effects. The prediction in Figure 13 consists of loading the CM6 test pile up to the set 1 load level, unloading and reloading, then applying the calibrated Carswell method to load set 1, before loading up to the load level of set 2 and again unloading and reloading. The solid-coloured lines show the response predicted for the hysteretic model, while the nonhysteretic model simply follows the backbone curve up and down. The measured loop shape of the first unload–reload loop from the CM6 test, for each load set, has been shifted and overlaid to match the numerical unload displacement. In effect, this removes the creep from the measured dataset. Furthermore, the secant stiffness for a full unload–reload using the three soil models and the experimental data has been plotted, starting from the maximum load point.

This comparison demonstrates that the secant stiffness of the nonhysteretic model is the lowest, followed by the hysteretic and then linear prediction. By taking the secant as a measure of the structural natural frequency, it is clear that the natural frequency predicted from the hysteretic method agrees very well with the measured data. Where in both sets of results, a cyclic recovery in stiffness associated with load reversals is observed. In contrast, the nonhysteretic method does not predict any static rotation at zero unload level; hence, the soil behaves overly soft, and the natural frequency is underestimated. In the linear elastic case, the stiffness is overpredicted when compared with the measured secant stiffness. Comparisons between these results in Figure 13 therefore provide evidence for the shifted peaks shown in Figure 12, where lower natural frequencies result in greater dynamic amplification from the low-frequency wind and wave excitations. Hence, the energy content shown in
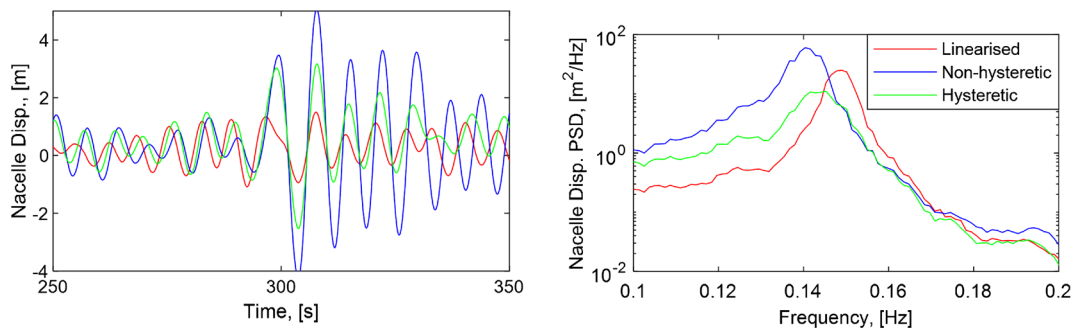

FIGURE 12   Nacelle displacement for DLC 6.1 (left, timeseries; right, PSD).
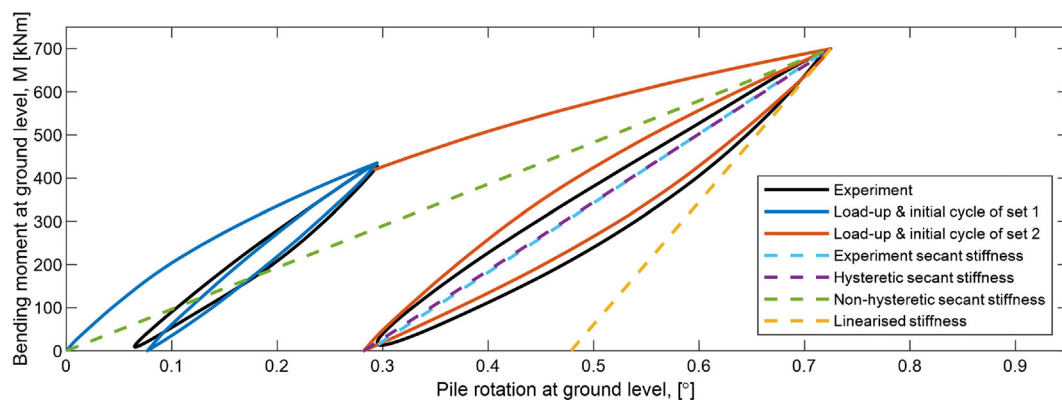

FIGURE 13   Comparison of predicted and measured moment-rotation responses for CM6 test pile for CM6 load levels 1 and 2, along with a comparison of measured secant stiffness to predictions using the hysteretic and nonhysteretic foundation modelling methods.

Figure 12 for the nonhysteretic model is significantly higher than the other models. In Figure 13, the unload path for the hysteretic method is different to the load path, meaning that the work done on the surrounding soil is larger than the elastic energy recovered upon unload, that is, some energy has been dissipated in the form of plastic deformation and internal material damping during load and unload. By taking the area of the enclosed loop as a measure of this damping, it is evident that the hysteretic model is able to reproduce similar nonlinear damping behaviour to that observed in the CM6 experimental results. This damping mechanism further explains why there is a large difference in energy content between the hysteretic and nonhysteretic methods shown in Figure 12. The comparison with CM6 test pile results gives confidence that both the stiffness and overall damping of the hysteretic method is more accurately matching the in situ physics than the linear or nonhysteretic models.

It is recognized that other experiments have shown that Masing rules overestimate the amount of damping especially at high strains, which may be an artefact of hardening or softening of the soil response. However, the loading on offshore wind turbines is such that the foundation rarely gets into this range of large damping. Evidence of this is presented in Figure 13, where good agreement between the hysteretic method and measured enclosed loop area is seen for a range of practical strains, for example, final rotations below 0.3°. Nevertheless, there are numerous approaches that capture this behaviour. One method would be the calibration of the hysteretic backbone curve to the response after many cycles, as predicted by the thermodynamically compliant model HARM.[2] Another method is outlined in Kaynia,[54] whereby an Iwan style multisurface plasticity method is coupled with elastic nonlinear springs. However, as stated in this paper, a drawback of this solution is that the inclusion of the nonlinear elastic springs means that the stiffness at unloading points can be less than the stiffness at loading points.

Further evidence of differences due to foundation modelling methods is shown in Figure 14. This shows the relative importance of each foundation model in terms of steel utilization ratios (UR), where the differences in foundation damping and stiffness for DLC 6.1 have a significant influence on the corresponding buckling and yielding checks. Approximately 20% reductions in steel utilization are seen when soil hysteresis is modelled for DLC 6.1, in comparison with the approach of including soil plasticity without capturing hysteretic behaviour (nonhysteretic PISA method). Importantly, this significant reduction in UR is seen from the monopile toe to the top of WTG tower. Hysteretic foundation modelling would therefore likely result in significant cost savings for an OWT project through reductions in steel required, for example, reduced monopile wall thickness, while also increasing the range of deployable water depths for monopile foundations.

However, the same magnitude of differences in results between each foundation modelling method is not observed for DLC 1.4. In DLC 1.4, the nonturbulent wind conditions rise over a 10 s duration which is a sufficiently longer time scale than the structural natural periods to not induce resonance effects. As result, this is most likely to represent a quasi-static load scenario whereby the foundation stiffness and damping do not play a significant role. While steel URs are still relatively high for DLC 1.4, which may mean that any reductions in DLC 6.1 URs could be non-critical, this study is based on just one set of metocean and soil conditions for a specific turbine. Different sites and turbines will have different governing DLCs; therefore, different benefits may be observed elsewhere. In particular, as the industry trend is to install OWTs in ever deeper waters, it is anticipated that severity of storms (DLC 6.1) will become more and more critical.

Figure 15 summarizes the check of foundation stability caused by extreme load events (DLC 6.1) including cyclic degradation effects. Note that the choice of foundation model effects both the design load and design soil capacity, where differences in the latter arise due to varying degrees of degradation obtained from the BSH storm load time history associated with each foundation model. By comparing the relative reductions in degradation (from black line to nonblack lines), there are significant differences in the design capacity of each model. These variations arise from differences in the response for the BSH storm load time history. This in turn is due to previously discussed variations in modelling approaches, that is, differences in soil damping and varying degrees of fidelity in terms of modelling foundation stiffness. Recent research in the offshore geotechnical industry suggests that the largest loads during a storm cause most of the degradation.[55] Therefore, as a measure of
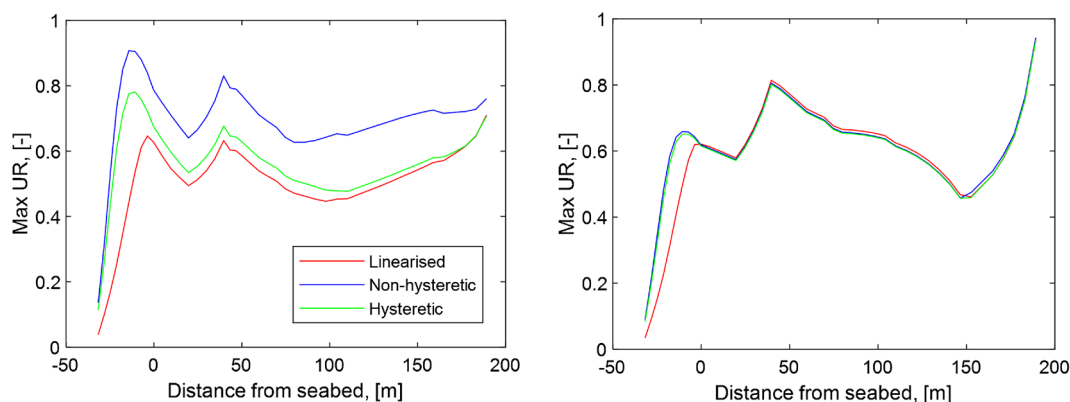
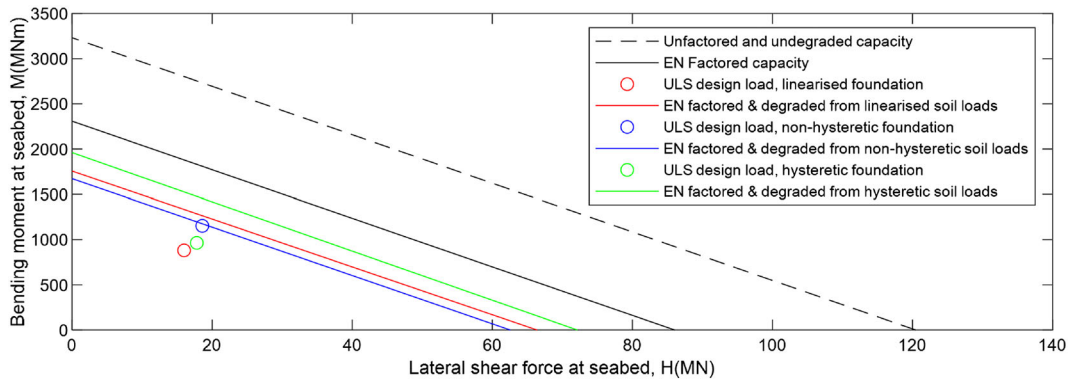**FIGURE 14** Steel utilization ratios (left, DLC 6.1; right, DLC 1.4).

FIGURE 15 Geotechnical failure envelope/ultimate load interaction diagram.

TABLE 8 Statistical properties of bending moments (M) at seabed for BSH storm analysis.

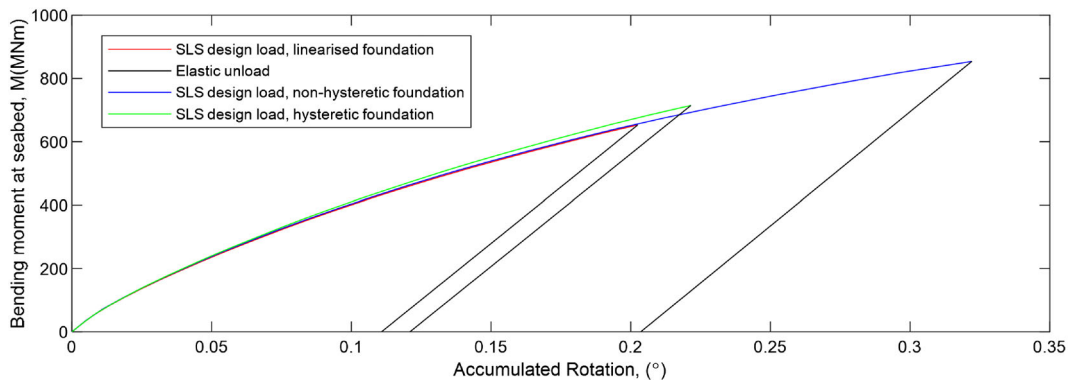| Property (−)	Linearized, M (MNm)	Nonhysteretic, M (MNm)	Hysteretic, M (MNm)
RMS of full BSH storm analysis	174	182	163
RMS of values above 95th percentile	380	402	348

FIGURE 16 Accumulated rotation at mudline.

the amount of degradation load level for each model, the root mean square (RMS) of the bending moments at seabed for the BSH storm analyses are shown in Table 8. Note that more than a 15% increase in RMS is observed for the largest 5% of loads when comparing the nonhysteretic case to the hysteretic case. Similar trends are also seen with the RMS for the full storm time series.

The effect of these differences in loading characteristics is twofold: Larger seabed loads lead to more degradation of ultimate capacity but also result in softer springs for DLC 6.1 which in turn leads to larger dynamic amplification and design loads. This effect is particularly important when comparing the industry standard approach of the nonhysteretic method against the hysteretic model. Subsequently, there are significant potential cost savings if a foundation model with hysteretic capabilities is included within a design framework, for example, reduced monopile embedment lengths.

Figure 16 summarizes the results from the SLS analysis. Similar to the load interaction diagram, the variation in degradation and design load for each foundation model has an important influence on the final accumulated rotation, where the former is evident from the difference in plasticity behaviour for each moment rotation curve and the latter is shown by the variation in peak load. Despite the use of a simplified accumulated rotation model, the relative difference in the response indicates that soil hysteresis has a significant impact on OWT design. In addition, small changes in peak load levels in the plastic regime result in large changes in accumulated rotation. Therefore, while the results are promising for cost savings, the exact magnitude of benefit will likely need to be considered in future research with a higher fidelity cyclic effect model such as HARM.[2]

5 | CONCLUSION

This paper presents a model for simulating offshore wind turbines using industry standard aero-hydro-servo-elastic methods that are fully coupled with a multisurface plasticity 1D Winkler foundation model. The aeroelastic capabilities are shown to be in good agreement with industry standard codes, such as OpenFAST. The inclusion of the multisurface plasticity foundation model has allowed investigation of the unknown influence of hysteretic soil reactions on ULS and SLS designs of offshore wind turbines, where hysteretic reactions inherently include soil damping as well as a more accurate representation of soil stiffness when compared with nonhysteretic methods used in industry, for example, p−y and linear springs. These hysteretic soil predictions are shown to be in good agreement with CM6 Cowden PISA test piles in terms of secant stiffness and amount of damping.[38] In contrast, the secant stiffness predicted using industry standard PISA-based p−y method is significantly underestimated. Therefore, the novelty in the paper lies in the coupling of realistic hysteretic soil reactions and the subsequent influence that this has on response and design. To conduct this analysis, the method developed by Carswell et al.[41] has been calibrated to match the accumulated rotation of the CM6 test pile cyclic results. Prior to any extreme event analysis, this cyclic model was used to quantify the soil degradation due to a 35 h design storm.[44]

Results from ULS load case time integration calculations demonstrate the importance of integrating aeroelastic codes with a foundation model capable of simulating real soil behaviour. Namely, the ULS extreme storm event analysis shows a 15% reduction in peak seabed bending moment when hysteretic soil reactions are included in comparison with the industry standard approach of nonlinear springs without hysteresis. Subsequently, 20% reductions in steel utilization are seen across the full monopile and turbine tower when hysteretic soil reactions are included.

Reductions in design loads are also observed for geotechnical design checks; however, in this case, the variation in soil degradation between each pile–soil interaction model means that differences in capacity also exist. The predicted accumulated rotation for the hysteretic model is almost 45% smaller than the nonhysteretic method. Similar observations exist for the pushover analysis, where the reduction in soil utilization is closer to 25% when hysteresis is included in comparison with the nonhysteretic approach. These findings suggest significant potential cost savings for an OWT project through reductions in steel required, while also increasing the range of deployable water depths for monopile foundations. It is noted that despite using a simplified cyclic degradation and ratcheting model, the relative difference in the response indicates that soil hysteresis has a significant impact on load calculation and cyclic soil response modelling. These effects are likely to be load case dependent and specific to each soil type despite the common approach in industry to assume a constant soil damping ratio project wide.

Future analysis will investigate the influence of hysteretic soil behaviour on fatigue limit state and look to incorporate findings within a design framework while focussing on efficiency.

DATA AVAILABILITY STATEMENT
The data that support the findings of this study are available from the corresponding author upon reasonable request.

ORCID
Gerard V. Ryan https://orcid.org/0009-0008-7472-7524

REFERENCES
1. Byrne BW. Lateral pile design for offshore wind turbines. In: *Piling 2020: Proceedings of the Piling 2020 Conference*. ICE Publishing; 2021:13-33.
2. Houlsby GT, Abadie CN, Beuckelaers WJAP, Byrne BW. A model for nonlinear hysteretic and ratcheting behaviour. *Int J Solids Struct*. 2017;120:67-80. doi:10.1016/j.ijsolstr.2017.04.031
3. Skau KS, Page AM, Kaynia AM, et al. REDWIN—REDucing cost in offshore WINd by integrated structural and geotechnical design. In *Journal of Physics: Conference Series*. Vol. 1104. IOP Publishing; 2018:012029.
4. Whyte SA, Burd HJ, Martin CM, Rattley MJ. Formulation and implementation of a practical multi-surface soil plasticity model. *Comput Geotech*. 2020;117:103092. doi:10.1016/j.compgeo.2019.05.007
5. Malekjafarian A, Jalilvand S, Doherty P, Igoe D. Foundation damping for monopile supported offshore wind turbines: a review. *Marine Struct*. 2021;77:102937. doi:10.1016/j.marstruc.2021.102937
6. Ömer Faruk H, Mutungi H. Assessment of simulation codes for offshore wind turbine foundations (Chalmers University of Technology, Division of Structural Engineering). 2016.

7. Popko W, Vorpahl F, Zuga A, et al. Offshore code comparison collaboration continuation (OC4), phase 1—results of coupled simulations of an offshore wind turbine with jacket support structure. In The Twenty-Second International Offshore and Polar Engineering Conference. OnePetro. 2012.

8. Abadie CN, Byrne B, Houlsby G, Burd H, McAdam R, Beuckelaers W. Modelling of offshore wind monopile lifetime performance. 2022.

9. Wichtmann T, Rondón HA, Niemunis A, Triantafyllidis T, Lizcano A. Prediction of permanent deformations in pavements using a high-cycle accumulation model. *J Geotech Geoenviron Eng*. 2010;136(5):728-740. doi:10.1061/(ASCE)GT.1943-5606.0000275

10. McAdam RA, Chatzis MN, Kulelia M, Anderson E, Byrne BW. Foundation stiffness estimation of an instrumented offshore wind turbine through model updating. 2023;2023:1-19. doi:10.1155/2023/4474809

11. Hassan G. *Bladed Theory Manual*. Co: Garrad Hassan & Partners Ltd; 2011.

12. Shabana AA. *Dynamics of Multibody Systems*. Cambridge university press; 2020.

13. Friedman Z, Kosmatka JB. An improved two-node Timoshenko beam finite element. *Comput Struct*. 1993;47(3):473-481. doi:10.1016/0045-7949(93)90243-7

14. Algolfat A, Wang W, Albarbar A. Study of centrifugal stiffening on the free vibrations and dynamic response of offshore wind turbine blades. *Energies*. 2022;15(17):6120. doi:10.3390/en15176120

15. Gavin H. In: Edmund T, ed. *Geometric Stiffness Effects in 2D and 3D Frames*. Department of Civil and Environment Engineering. Pratt School of Engineering, Duke University; 2012:1-14.

16. Clough RW, Penzien J. *Dynamics of structures, computers & structures*. New York; 1995.

17. Chopra AK. *Dynamics of Structures*. fourth ed. Prentice Hall; 2012.

18. BS EN IEC 61400-3 wind turbines—part 3: design requirements for offshore wind turbines. 2019.

19. Sobey RJ. Wave theory predictions of crest kinematics. In: *Water Wave Kinematics*. Springer; 1990:215-231. doi:10.1007/978-94-009-0531-3_13

20. Wheeler JD. Method for prediction of forces produced by irregular waves. In *Offshore Technology Conference*. Houston, TX, USA; 1969.

21. Dean RG. Stream function representation of nonlinear ocean waves. *J Geophys Res*. 1965;70(18):4561-4572. doi:10.1029/JZ070i018p04561

22. Hansen MOL. *Aerodynamics of Wind Turbines*. Routledge; 2015. doi:10.4324/9781315769981

23. Bak C, Madsen HA, Johansen J. Influence from blade-tower interaction on fatigue loads and dynamics. In 2001 European Wind Energy Conference and Exhibition (EWEC'01). WIP-Renewable Energies; 2001:394-397.

24. Glauert H. *The Analysis of Experimental Results in the Windmill Brake and Vortex Ring States of an Airscrew*. HM Stationery Office; 1926.

25. Glauert H. Airplane Propellers, In: Durand WF, ed. *Aerodynamic Theory*. Division L; 1935. doi:10.1007/978-3-642-91487-4_3

26. Øye S. Induced velocities for rotors in yaw. In: *Proceedings of the Sixth IEA Symposium*. Energy Research Centre of the Netherlands; 1992:1-5.

27. Hansen MH, Gaunaa M, Madsen HA. A Beddoes-Leishman type dynamic stall model in state-space and indicial formulations; 2004.

28. Øye S. Tjæreborg wind turbine: 4. Dynamic inflow measurement; 1991.

29. Jonkman BJ, Buhl Jr ML. Turbsim user's guide Tech. rep. National Renewable Energy Lab.(NREL), Golden, CO (United States); 2006.

30. Abbas NJ, Zalkind DS, Pao L, Wright A. A reference open-source controller for fixed and floating offshore wind turbines. *Wind Energy Sci*. 2022;7(1):53-73. doi:10.5194/wes-7-53-2022

31. Newmark NM. A method of computation for structural dynamics. *J Eng Mech Div*. 1959;85(3):67-94. doi:10.1061/JMCEA3.0000098

32. Géradin M, Cardona A. *Flexible Multibody Dynamics: A Finite Element Approach*. Wiley; 2001.

33. Jonkman J, Musial W. Offshore code comparison collaboration (OC3) for IEA Wind Task 23 offshore wind technology and deployment (No. NREL/TP-5000-48191). National Renewable Energy Lab.(NREL), Golden, CO (United States); 2010.

34. Jonkman J, Butterfield S, Musial W, Scott G. Definition of a 5-MW reference wind turbine for offshore system development (No. NREL/TP-500-38060). National Renewable Energy Lab.(NREL), Golden, CO (United States); 2009.

35. Byrne BW, Houlsby GT, Burd HJ, et al. PISA design model for monopiles for offshore wind turbines: application to a stiff glacial clay till. *Géotechnique*. 2020;70(11):1030-1047. doi:10.1680/jgeot.18.P.255

36. Byrne BW, McAdam RA, Burd HJ, et al. Monotonic laterally loaded pile testing in a stiff glacial clay till at Cowden. *Géotechnique*. 2020;70(11):970-985. doi:10.1680/jgeot.18.PISA.003

37. Gaertner E, Rinker J, Sethuraman L, et al. Definition of the IEA wind 15-megawatt offshore reference wind turbine technical report. 2020.

38. Byrne BW, McAdam RA, Beuckelaers WJ, et al. Cyclic laterally loaded medium scale field pile testing for the PISA project. In 4th International Symposium on Frontiers in Offshore Geotechnics; 2020:1323-1332.

39. API (American Petroleum Institute). *RP 1A-WSD—Recommended Practice for Planning, Designing and Constructing Fixed Offshore Platforms*. API; 2010.

40. Andersen, K.H., 2009. Bearing capacity under cyclic loading—offshore, along the coast, and on land. The 21st Bjerrum Lecture presented in Oslo, 23 November 2007. *Canadian Geotechnical Journal*, 46(5), pp.513-535.

41. Carswell W, Arwade SR, DeGroot DJ, Myers AT. Natural frequency degradation and permanent accumulated rotation for offshore wind turbine monopiles in clay. *Renew Energy*. 2016;97:319-330. doi:10.1016/j.renene.2016.05.080

42. Leblanc C, Byrne BW, Houlsby GT. Response of stiff piles to random two-way lateral loading. *Géotechnique*. 2010;60(9):715-721. doi:10.1680/geot.09.T.011

43. DNVGL (Det Norske Veritas–Germanischer Lloyd). *DNVGL-RP-C212: Offshore Soil Mechanics and Geotechnical Engineering*. DNV GL; 2021.

44. BSH. Minimum requirements concerning the constructive design of offshore structures within the exclusive economic zone (EEZ) (National Standard No. 7005). BSH; 2015.

45. Rainey PJ, Camp TR. Constrained nonlinear waves for offshore wind turbine design. In *Journal of Physics: Conference Series*. Vol. 75. IOP Publishing; 2007:012067. doi:10.1088/1742-6596/75/1/012067

46. DNVGL (Det Norske Veritas–Germanischer Lloyd). *DNVGL-ST-0126: Support Structures for Wind Turbines*. DNV GL; 2016a.

47. DNVGL (Det Norske Veritas–Germanischer Lloyd). *DNVGL-RP-C202: Buckling Strength of Shells*. DNV GL; 2019a.

48. BS EN 10025-2. Hot rolled products of structural steels—part 2: technical delivery conditions for non-alloy structural steels. 2019.

49. EN 1997-1. Eurocode 7 geotechnical design—part 1: general rules. 2004.

50. DNVGL (Det Norske Veritas–Germanischer Lloyd). *DNVGL-ST-0437: Loads and Site Conditions for Wind Turbines*. DNV GL; 2016b.

51. Shirzadeh R, Weijtjens W, Guillaume P, Devriendt C. The dynamics of an offshore wind turbine in parked conditions: a comparison between simulations and measurements. *Wind Energy*. 2015;18(10):1685-1702. doi:10.1002/we.1781

52. Kelley ND, Jonkman BJ. Overview of the TurbSim stochastic inflow turbulence simulator (No. NREL/TP-500-36971). National Renewable Energy Lab. (NREL), Golden, CO (United States); 2005.

53. DNVGL (Det Norske Veritas–Germanischer Lloyd), 2019. *DNVGL-RP-C205: Recommended practice environmental conditions and environmental loads*. DNV GL: Oslo, Norway.

54. Kaynia AM. Seismic considerations in design of offshore wind turbines. *Soil Dyn Earthq Eng*. 2019;124:399-407. doi:10.1016/j.soildyn.2018.04.038

55. Zhang Y, Andersen KH, Jeanjean P. Cyclic py curves in clays for offshore structures. In Offshore Technology Conference. OnePetro. 2019.